

Bai, Y., Yuan, X., He, Y., Hou, G., Thant, M., Sein, K., Ai, Y. (2020):
Mantle Transition Zone Structure Beneath Myanmar and Its
Geodynamic Implications. - Geochemistry Geophysics Geosystems
(G3), 21, 12, e2020GC009262.

<https://doi.org/10.1029/2020GC009262>

Geochemistry, Geophysics, Geosystems

RESEARCH ARTICLE

10.1029/2020GC009262

Key Points:

- Mantle discontinuities beneath Myanmar are imaged using P-wave receiver functions from dense regional seismic networks
- Depth variations of the 410 and 660-km discontinuities indicate interaction of the subducted Indian slab with the mantle transition zone
- Spatial offset between the 410-km discontinuity uplift and the 660-km discontinuity depression implies slab break-off and tearing

Supporting Information:

- Supporting Information S1
- Table S1

Correspondence to:

Y. Ai,
ysai@mail.iggcas.ac.cn

Citation:

Bai, Y., Yuan, X., He, Y., Hou, G., Thant, M., Sein, K., & Ai, Y. (2020). Mantle transition zone structure beneath Myanmar and its geodynamic implications. *Geochemistry, Geophysics, Geosystems*, 21, e2020GC009262. <https://doi.org/10.1029/2020GC009262>

Received 19 JUN 2020

Accepted 19 NOV 2020

Mantle Transition Zone Structure Beneath Myanmar and Its Geodynamic Implications

Yiming Bai^{1,2,4} , Xiaohui Yuan² , Yumei He^{1,3,4}, Guangbing Hou¹, Myo Thant⁵, Kyaing Sein⁶, and Yinshuang Ai^{1,3,4} 

¹Key Laboratory of Earth and Planetary Physics, Institute of Geology and Geophysics, Chinese Academy of Sciences, Beijing, China, ²Deutsches GeoForschungsZentrum GFZ, Potsdam, Germany, ³University of Chinese Academy of Sciences, Beijing, China, ⁴CAS Center for Excellence in Tibetan Plateau Earth Sciences, Beijing, China, ⁵Department of Geology, University of Yangon, Yangon, Myanmar, ⁶Myanmar Geosciences Society, Yangon, Myanmar

Abstract Linking the India-Tibet collision to the north and the Andaman oceanic subduction to the south, Myanmar occupies a crucial position in the India-Eurasia convergence system. Various seismological studies have indicated that the Indian plate is obliquely subducted along the Burma arc. However, the depth extent and continuity of the subducted slab remain enigmatic. With seismic recordings collected from 114 recently deployed seismic stations, we map the topographies of the mantle transition zone (MTZ) boundaries, that is, the 410- and 660-km discontinuities, beneath Myanmar using receiver functions. Regional 3-D velocity models were adopted to account for the lateral velocity heterogeneity. The 410-km discontinuity is uplifted by over 15 km within 95°E–97°E and 21°N–24°N beneath Myanmar. This feature correlates well with the east-dipping high-velocity anomaly in the tomographic models, with a velocity increase of 0.9%–1.2% at the 410-km discontinuity depth, suggesting that the subducted slab has reached the MTZ. The uplift of the 410-km discontinuity terminates to the south at ~21°N, indicating a distinct change in slab geometry. Our results also reveal a depressed 660-km discontinuity, which is spatially offset to the southwest of the uplifted 410-km discontinuity. We propose that the offset between the 410-km discontinuity uplift and the 660-km discontinuity depression could indicate a slab break-off and tearing beneath Myanmar, which was triggered by the northward motion of the Indian plate during the eastward subduction. We further speculate that the slab tear could mark the transition from oceanic to continental plate subduction.

Plain Language Summary The complex tectonic activities in Myanmar are largely dominated by highly oblique eastward subduction of the Indian plate. So far, the depth and continuity of the Indian plate that is subducted deeply beneath Myanmar remain unclear. The present work focuses on the mantle transition zone (MTZ) in order to trace the subducting Indian slab. Based on seismic data collected from 114 recently installed broadband stations in Myanmar, we use seismic P-to-S converted waves to map the topographies of the MTZ interfaces, that is, the 410- and 660-km discontinuities. We observe a localized uplift of the 410- and a depression of the 660-km discontinuity, and the two anomalies are horizontally offset by ~120 km. Since the depths of these discontinuities are sensitive to temperature, our observations indicate that the MTZ structure is affected by the cold subducted slab. Integrating with previous studies, we confirm the arrival of the Indian slab into the MTZ beneath Myanmar and further suggest the occurrence of a slab break-off and tearing during the eastward subduction. Our results provide important constraints on the subduction geometry as well as the fate of the eastward subducted Indian slab.

1. Introduction

Following the closure of the Neo-Tethys ocean, the Indian plate began to collide with the Eurasian plate in the Eocene (e.g., Molnar & Stock, 2009). One of the profound consequences is the formation of the Himalayan mountain belt and the Tibetan plateau. The convergent boundary extends along the Himalayan arc and is terminated to the east at the eastern Himalayan syntaxis, where it bends to the south, continues along the Burma arc, and connects to the Andaman-Sumatra arc, a site of oceanic subduction. While many seismic experiments have demonstrated that the Indian lithosphere is underthrusting northwards under Tibet (e.g., Kind et al., 2002; Nábělek et al., 2009), the detailed subduction geometry

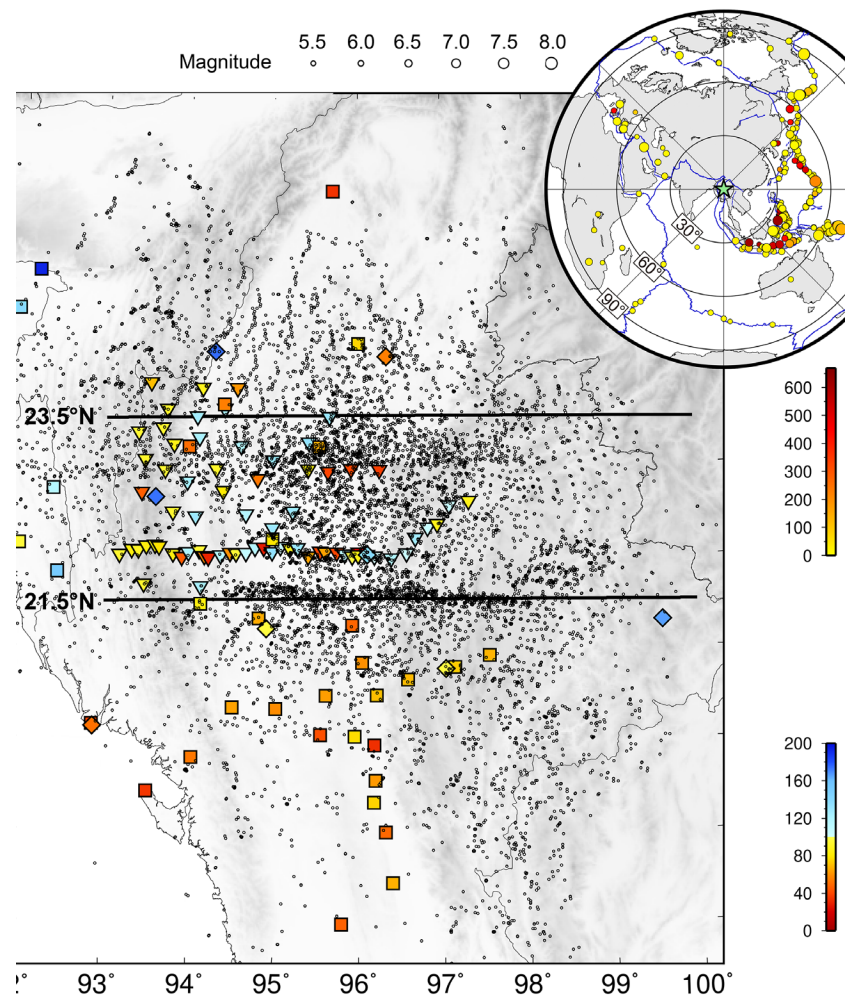


Figure 1. Overview map of the study region, showing topography, seismic stations, Holocene volcanoes, major faults (Taylor & Yin, 2009), and relocated seismicity (ISC-EHB Bulletin 1964–2016, Engdahl et al., 2020). Iso-depth contours of the subducted Indian slab are from the slab2 model (Hayes et al., 2018). Tectonics of SE Asia is shown in the inset map. The red rectangle outlines the present study region. The blue arrow denotes the plate motion of India relative to Eurasia in the HS3-NUVEL 1A model (Gripp & Gordon, 2002).

at the eastern flank of the convergent zone is still under debate. The present work aims to constrain the subduction geometry by looking into the interaction of the subducted slab with the mantle transition zone (MTZ).

Our study region lies mainly in Myanmar and can be structurally divided into three north-south elongated tectonic blocks (Figure 1): (1) The Indo-Burma Ranges have been inferred as an active accretionary wedge resulting from the eastward subduction of the Indian oceanic crust (e.g., Maurin & Rangin, 2009). (2) The Central Myanmar Basin, bounded to the east of the Indo-Burma Ranges by the Kabaw fault, is a series of Cenozoic basins filled up with up to 15 km of sediments and with sparse volcanism on the surface (Maurin & Rangin, 2009; A. H. G. Mitchell, 1993). These two blocks form the Burma plate, which is moving northwards with the Indian plate along the ~1,200 km long dextral Sagaing fault (Maurin et al., 2010). (3) The Shan Plateau, with an average elevation of 1 km, is the west edge of the Indochina Peninsula separated from the Burma plate by the Mogok metamorphic belt (A. Mitchell et al., 2012).

Below the Burma plate, a well-defined Wadati-Benioff zone extending down to a depth of ~180 km indicates the presence of eastward subduction of the Indian slab (e.g., Hurukawa et al., 2012; Ni et al., 1989; Figure 1). Global and regional tomographic results, although with considerably different resolution

and depth extent, have all revealed an east-dipping, slab-like high-velocity structure descending far beyond the Wadati-Benioff depth into the upper mantle (e.g., Huang & Zhao, 2006; Koulakov, 2011; Lei & Zhao, 2016; Li, van der Hilst, Meltzer, & Engdahl, 2008; Replumaz et al., 2004; van der Meer et al., 2018; Wei et al., 2012; Figure S1). Li, van der Hilst, Meltzer, and Engdahl (2008) show that the Indian slab subducts eastwards in the upper mantle and becomes elusive at ~500 km depth in the MTZ. This result is confirmed by Koulakov (2011) with increased resolution by using the earthquakes beneath Myanmar recorded by global stations. In Wei et al. (2012), a continuous slab appears to extend down to the bottom of the MTZ under the South China block. Pesicek et al. (2010) observed a continuous slab south of 22°N and a broken one with a gap in the MTZ north of it. The discrepancy in the observed slab geometry may largely be attributed to the sparse distribution of seismic stations in the region, especially in Myanmar.

The topographies of the 410- and 660-km discontinuities (D410 and D660, hereafter) that define the top and bottom of the MTZ can provide crucial evidence on the deep structure of the subducted slab. These two discontinuities are generally assumed to be caused by mineral phase transformations of olivine (α -spinel) to wadsleyite (β -spinel) and ringwoodite (γ -spinel) to perovskite (also known as bridgmanite) and magnesiowüstite, respectively (e.g., Bina & Helffrich, 1994). Mineral physics studies indicate that both reactions depend on the temperature but with opposite Clapeyron slopes (pressure-temperature dependence) (Helffrich, 2000). It means that a low temperature in the MTZ, such as that caused by the addition of a cold subducted slab, would result in an uplift of the D410 and a depression of the D660, hence a thickened MTZ. Similarly, a high temperature would cause a thinned MTZ.

Depth variations of the MTZ discontinuities and the corresponding MTZ thickness have been observed globally using seismological techniques such as receiver functions (RFs) (e.g., Lawrence & Shearer, 2006), SS and PP precursors (e.g., Houser et al., 2008; Lawrence & Shearer, 2008). Unfortunately, global MTZ structure does not have sufficient resolution to constrain the slab geometry beneath Myanmar. Regional studies of MTZ discontinuities mainly focused on the adjacent regions, where seismic stations are abundant, such as beneath the Tibetan plateau (e.g., Duan et al., 2017; Saikia et al., 2020; Xu et al., 2018; Zhang et al., 2017) and the Indochina block (Yu et al., 2017). Recent RF studies suggest that the eastward subducted Indian plate may have experienced a break-off or tearing process (Xu et al., 2018; Zhang et al., 2017). Where this break-off occurred remains unclear, mainly because most seismic stations they used are located away from the subduction front. A detailed study of the MTZ structure beneath Myanmar requires regional seismic stations.

In this study, we calculate P-wave RFs with waveforms from newly deployed seismic networks to detect detailed structure of the MTZ beneath Myanmar and its surrounding regions. The resulting RF images reveal significant variations in the MTZ discontinuity depths, which provide constraints on the slab geometry and implications for the subduction dynamics.

2. Data and Methods

2.1. Seismic Networks

A portable array of 71 stations with a spacing of 15–40 km were deployed in June 2016 under the China-Myanmar Geophysical Survey in the Myanmar Orogen (CMGSMO) project and acquired over 1 year of continuous seismic data (Mon et al., 2020). Each station was equipped with a Güralp CMG-3ESP or a Nanometrics Trillium 120PA seismometer and a Trimble Ref Tek 130 digitizer with sampling rate of 40 Hz. In addition to the CMGSMO seismic network, we included 34 stations operated by the Earth Observatory of Singapore since October 2016, with an average spacing of ~150 km (Wang et al., 2019). The remaining nine stations belong to the Myanmar National Seismic Network and were requested from the Incorporated Research Institutions for Seismology Data Management Center. Overall, 114 broadband seismic stations in Myanmar and its adjacent region are gathered to investigate the MTZ structure beneath Myanmar (Figure 2 and Table S1).

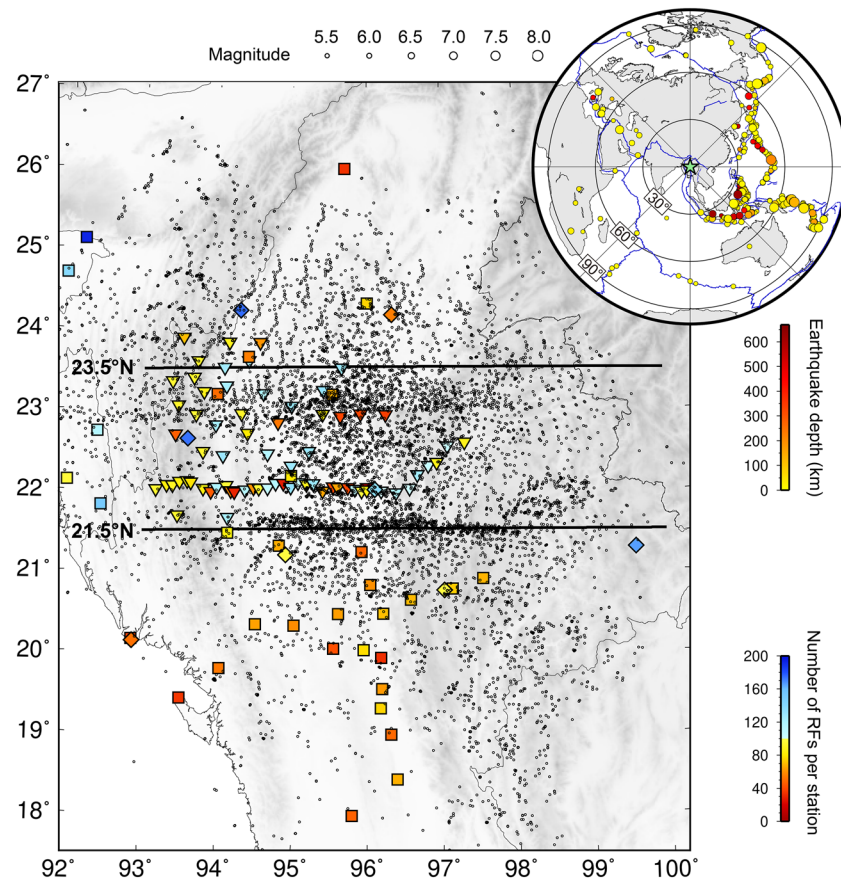


Figure 2. Map showing data coverage of this study. Triangles, squares, and diamonds are seismic stations (also see Figure 1). Colors of symbols denote number of RFs associated with each station. Black circles are Ps piercing points in the middle depth of the MTZ at 540 km. Two thick lines indicate CCP stacked profiles along latitudes 21.5°N and 23.5°N. Four-hundred and fifty-seven teleseismic events used in this study are shown as circles in the inset map, with sizes and colors representing earthquake magnitude and depth, respectively.

2.2. Receiver Functions

P-wave RFs are time series containing P-to-S conversions and multiple reverberations generated at seismic velocity discontinuities (Langston, 1979; Vinnik, 1977), which have proven to be effective for imaging the mantle discontinuities (e.g., Kind et al., 2002). For RF analysis, we selected earthquakes with magnitude larger than 5.5 and epicentral distance between 30° and 90°. Seismograms with signal-to-noise ratio lower than 3.0 and those showing strong interference with other phases were discarded during manual inspection. The signal-to-noise ratio in this study is defined as A_S/A_N , where A_N and A_S are absolute maximum amplitude in the time window of 30 s before and after theoretical P arrivals on the vertical component. The calculation of RFs mainly includes two steps. First, to separate direct P and converted S phases from each other, the Z-N-E component seismograms are rotated into the P-SV-SH ray-based system, during which the theoretical incidence angle and back azimuth for each event are calculated using the global IASP91 velocity model (Kennett & Engdahl, 1991). Second, a time-domain spiking deconvolution is performed (Berkhout, 1977). During this process, an inverse filter is obtained by minimizing the least squares difference between the observed P component and a desired delta-like spike, and is convolved with the SV component in order to generate the source equalized RF. A band-pass filter of 3–30 s was applied to the resulting RFs.

We have obtained a total of 9,954 RFs. Figure 3a shows stacks of RFs of all stations in bins of epicentral distances of 0.5°. Primary converted phases from the Moho, the D410, and the D660 can be clearly identified throughout the entire distance range. Some multiple phases can also be recognized, which show different slowness. The primary conversions and the multiples can be identified and separated by the slant-stacking

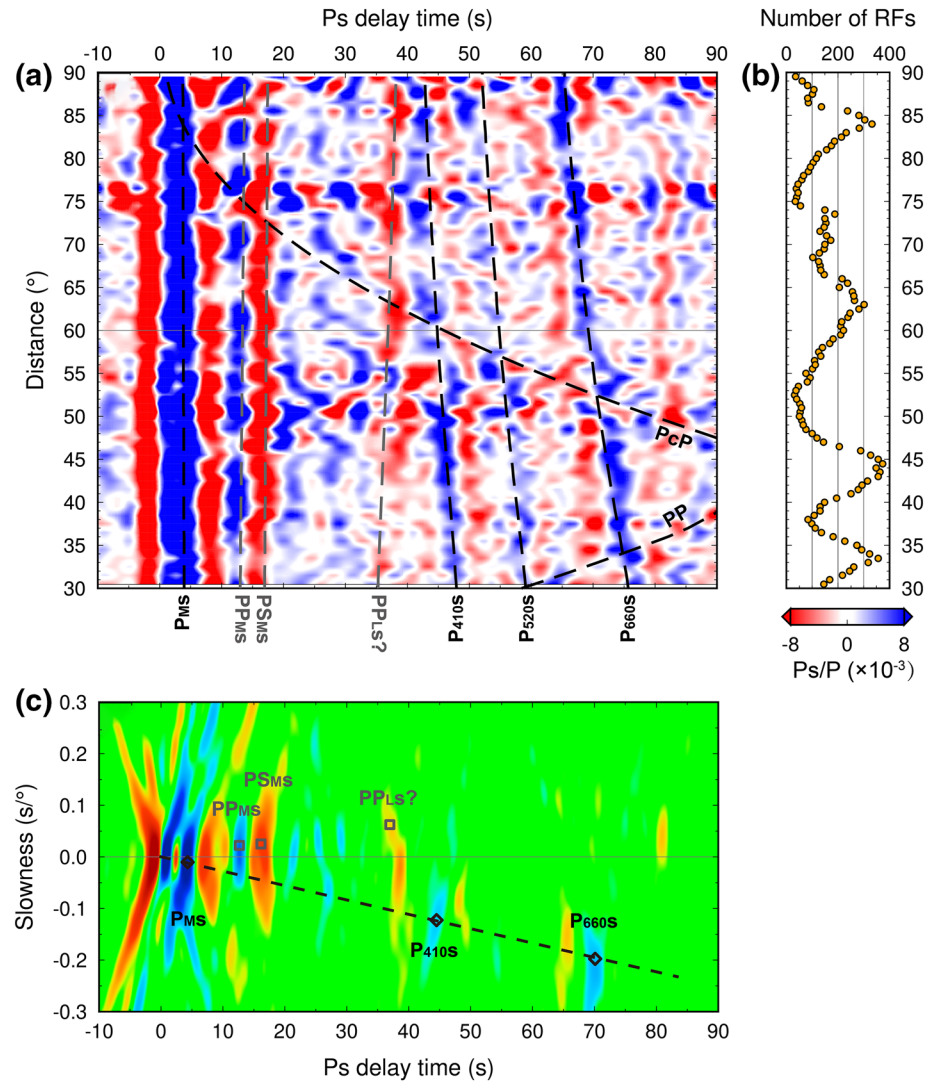


Figure 3. (a) Stacks of P-wave RFs collected from all stations in each 0.5° bin of epicentral distance. Dashed lines denote theoretical arrival times for different phases predicted with the reference 1-D IASP91 model (Kennett & Engdahl, 1991). P_{MS} , P_{410S} , and P_{660S} are Ps conversions generated at the Moho, the D410, and the D660. PP_{MS} and PS_{MS} are multiple phases generated at the Moho. $PP_{LS?}$ could possibly represent the multiple phase generated at the Eurasian LAB, the primary conversion of which is masked by the strong Moho multiples. (b) The number of RFs in different epicentral distance bins. (c) Slant-stacks of RFs. Positive and negative amplitudes are shaded in blue and red, respectively. The dashed line denotes theoretical slowness of Ps conversions. Diamonds and squares mark Ps converted phases and multiple reverberations, respectively. See text for more details.

method (X. Shen et al., 2014). By stacking RF amplitudes along different slowness, we can distinguish the converted Ps phase from the multiples. The range of slowness in this study is chosen to be -0.3 to 0.3 $s/^\circ$, which covers all the possible Ps phases converted at the D660 and above. Figure 3c shows the slant-stacked result of all RFs used in this study. The P-to-S conversions and multiple reverberations have a negative and positive relative slowness with respect to the direct P phase, respectively. The converted phases from the Moho, the D410, and the D660 are well recognized in the negative slowness domain. The 520 km discontinuity, which can be seen in the stacked RF map (Figure 3a), is barely visible in the slant-stacked map (Figure 3c), probably due to its smaller amplitude and broader depth variation in this area. Furthermore, a multiple signal can be seen between 35 and 40 s in the positive slowness domain which might represent the first multiple (PPs) of a downward velocity decrease, possibly the lithosphere-asthenosphere boundary (LAB) of the overriding Eurasian plate at ~ 100 km depth.

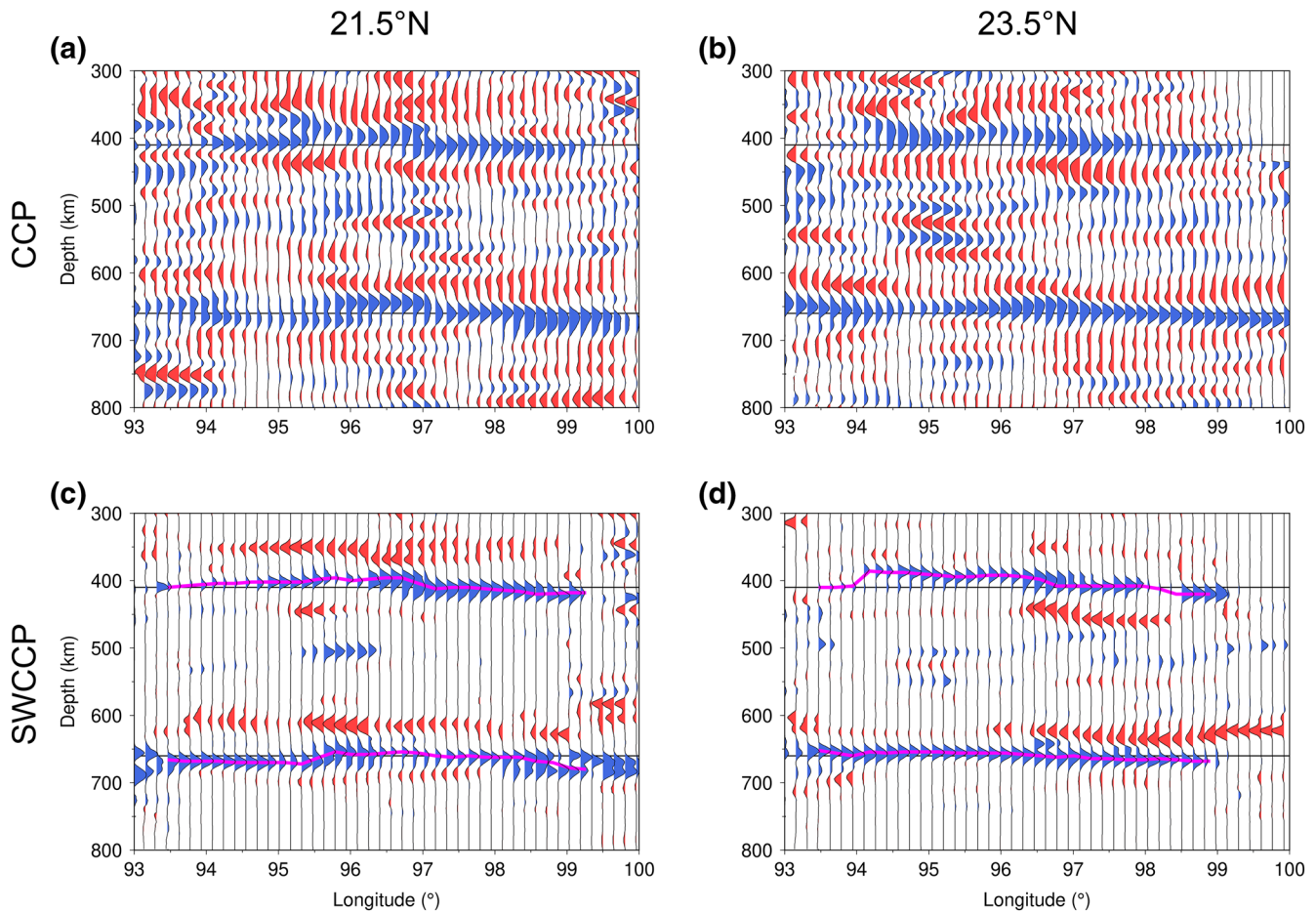


Figure 4. (a, b) CCP and (c, d) SWCCP stacked profiles constructed with the 1-D IASP91 model (Kennett & Engdahl, 1991) along (a, c) 21.5°N and (b, d) 23.5°N. Positive amplitudes, representing seismic discontinuities with increasing velocity with depth, are shaded in blue; negative amplitudes, representing discontinuities with decreasing velocity with depth, are in red. Purple lines in (c, d) denote apparent depths picked for the D410 and the D660.

2.3. Common Conversion Point Stacking

To transform RF time series into depth and to improve the spatial resolution, we adopted a common conversion point (CCP) stacking approach (e.g., Kind et al., 2002). Each amplitude on RFs was back-projected to its raypath position using a global 1-D velocity model, that is, the IASP91 velocity model (Kennett & Engdahl, 1991) in our case. Two depth profiles along 21.5°N and 23.5°N were assigned according to the coverage of Ps piercing points at MTZ depths (Figure 2). Each profile was divided into bins with spatial intervals of 4 km along the profile and 2 km in depth. All amplitudes in the same bin within a half-width of 1° on each side of the profile were stacked and normalized. A smoothing filter within one Fresnel zone was employed along the profile (Figures 4a and 4b).

Converted phases can be observed around the depths of 410 and 660 km. However, they are interfered with noise and multiple reverberations from the crust and shallow mantle in the CCP stacking traces, causing misidentification of the real MTZ phases. The D410 seems to be uplifted between 95°E and 97°E in both profiles. Depths of the D410 are generally hard to identify, especially west of 97°E, where several branches of positive phases interfere. The D660 is relatively easier to pick but it shows clearly different depth variations along two profiles. To reduce the influence of the multiples in our CCP profiles, we performed the slowness weighted CCP (SWCCP) stacking method (Guan & Niu, 2017). A slowness-based factor is designed to weight RF amplitudes along the CCP profile mainly according to the difference between the relative slowness of the slant-stacked amplitude and the theoretical slowness of the direct Ps

conversion (e.g., Figure 3c) (see Text S1 in supporting information for more details). Figures 4c and 4d show the corresponding SWCCP stacked results for the south (along 21.5°N) and north (along 23.5°N) profiles, respectively. It is obvious that the SWCCP stacks are much cleaner than the traditional CCP stacks. Many multiple phases have been removed or reduced, whereas the primary converted phases from the D410 and D660 are enhanced.

2.4. Correction for 3-D Velocity Heterogeneity

In order to map the 3-D depth variations of the MTZ discontinuities, the whole study region was divided into grids with spacing of 0.5° by 0.5° horizontally and 2 km vertically. We searched for all the back-projected RFs that are located within a circular area around each grid node. The radius of the searching area is 75 km for the D410 and 100 km for the D660, respectively, which corresponds approximately to the dimensions of the Fresnel zone and hence the lateral resolution of our data at MTZ depths. Grids with less than 50 RFs (Figure S2) were rejected to minimize the possibility of misidentifying the MTZ discontinuities. We then calculated the average amplitude at each grid and picked the maximum amplitude in depth windows of ± 40 km around 410 and 660 km. We followed the bootstrap method (Efron & Tibshirani, 1986) to resample the RF data set 200 times. The standard deviation of the discontinuity depth for most grids is no more than 2 km (Figure S2). Note that the 1-D IASP91 velocity model used for CCP stacking can only result in apparent depths of MTZ discontinuities rather than true depths.

The study region is very heterogeneous. Subducted slabs with high velocity anomalies in the mantle may affect the time-depth conversion of the Ps converted phases. To take into account the influence of lateral velocity heterogeneity, we back-projected individual RF time series into depth using 1-D velocity structures extracted in a 3-D model along raypaths (Eagar et al., 2010). A regional tomographic model (Koulakov, 2011) was employed to account for the mantle velocity effects. Because of missing seismic stations in Myanmar, Koulakov (2011) applied an inversion scheme by making use of earthquakes in the study area, which were recorded by global stations. This approach can increase the resolution of tomography from global to regional scales and is useful for subduction zones where earthquakes are abundant. This model has $\sim 2^\circ$ spatial resolution covering the entire study region. We only adopted the 3-D P-wave velocity perturbation ($d\ln V_p$) from Koulakov (2011), as the slab geometry is poorly resolved in the S-wave velocity model. Instead, the S-wave velocity perturbation ($d\ln V_s$) was estimated based on an average $d\ln V_s/d\ln V_p$ ratio of 1.73 for the upper mantle (Cammarrano et al., 2003; Yuan et al., 2017). The $d\ln V_p$ and $d\ln V_s$ were then converted to absolute velocities by perturbing the reference IASP91 model. Since the 3-D tomographic model (Koulakov, 2011) only involves the Moho depth to account for the crustal structure, the effect of thick sediments in the Central Myanmar Basin could be potentially underestimated. To enhance the contribution of the crustal-scale structure, we replaced the uppermost 80 km of the 3-D tomographic model by a recent crustal model in Myanmar region (Myanmar Hybrid version 1, Wang et al., 2019). This model reveals first-order basin and crustal structures, and agrees well with former geological and geophysical constraints. The 3-D velocity model used for CCP stacking thus takes both crustal and upper mantle velocity variations into consideration.

In Figure 5a, we compare the CCP stacks after taking into account the 3-D velocity variations with the P-wave tomographic model (Koulakov, 2011) along the north profile. The high-velocity anomaly correlates well with the D410 uplift. Figure 5b displays an example of time corrections to the Ps delay time induced by velocity anomalies within different depth ranges. The slab-related high-velocity anomaly in the upper mantle could reduce the Ps delay time, estimated with the IASP91 model, by over 1 s at some locations, roughly equivalent to +10 km depth correction to the D410 and the D660. By contrast, velocity anomalies within the crust and the MTZ have less effect on the time-depth conversion of the Ps converted phases. Figures 5c and 5d show depth variations of the D410 and the D660 along 23.5°N before and after taking into account the 3-D heterogeneity. Apparently, the two discontinuities are simultaneously deepening east of $\sim 96^\circ\text{E}$ after the high-velocity anomaly in the mantle is considered. The corresponding MTZ thickness, however, is less influenced by the 3-D velocity heterogeneity (Figure 5e; more CCP stacked profiles corrected for 3-D velocity effects are shown in Figure S3).

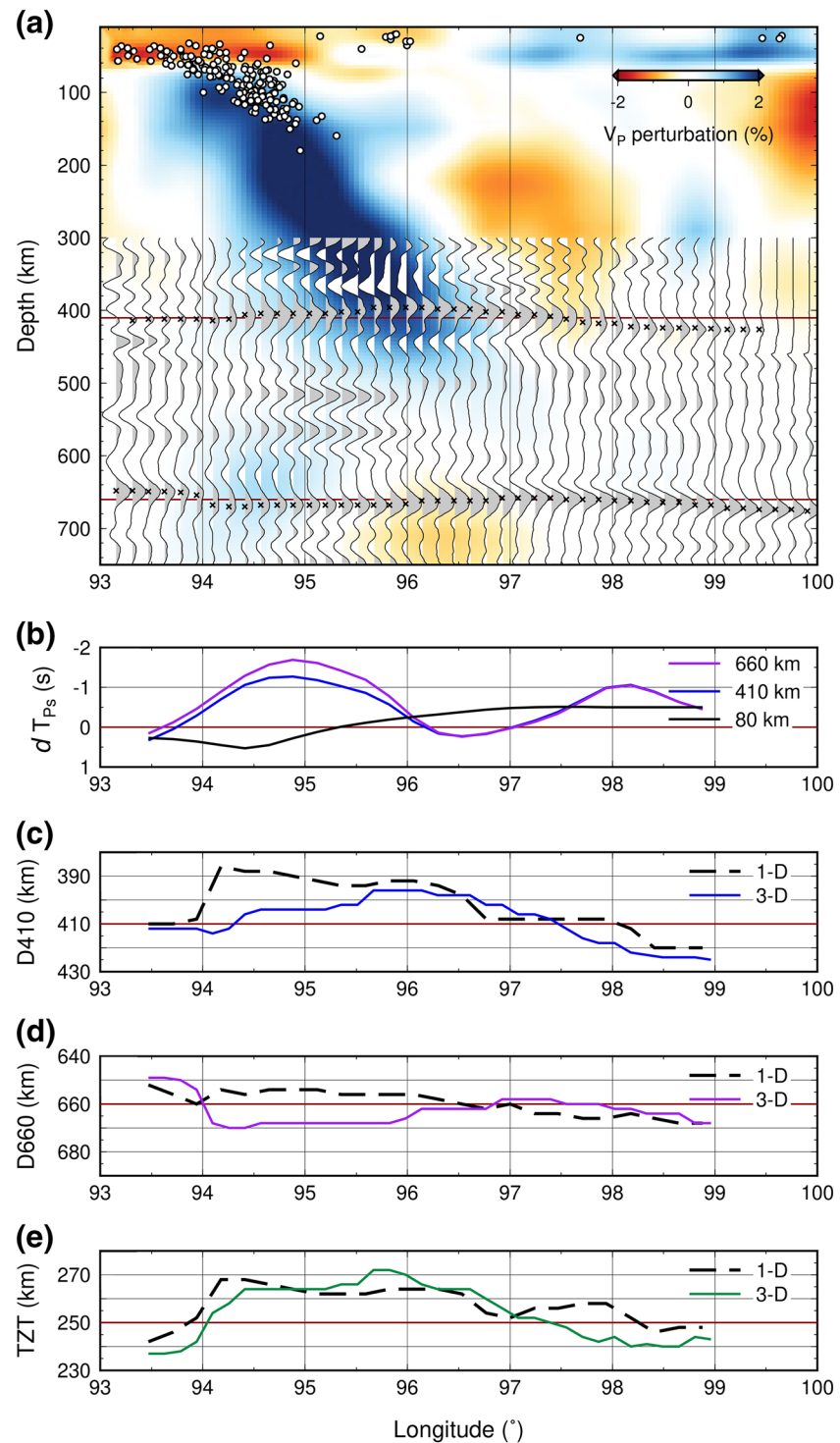


Figure 5. (a) Superposition of the CCP stacked profile after 3-D velocity correction with P-wave velocity perturbation (Koulakov, 2011) along 23.5°N. Black crosses indicate Ps conversions of the D410 and the D660. White dots denote relocated earthquakes within 23.5°N \pm 1° (Engdahl et al., 2020). (b) Example of time corrections (dT_{Ps}) to the IASP91 based Ps delay time due to 3-D velocity anomalies from the surface to the three different depths. For illustration purpose, at each geographical point, the velocity structures required for the Ps timing correction were sampled in the 3-D model along the ray paths, assuming an epicentral distance of 60° and a back azimuth of 90°. (c–e) Comparisons of depths of the D410 and the D660 and MTZ thicknesses (TZT) determined with the 1-D and 3-D velocity models.

3. Results

The SWCCP stacks helped enhance the primary converted phases and reduce the influence of multiples. In addition to the D410 and the D660, which are the main objects of the present study, several negative phases are preserved by the slowness weighted algorithm. The negative signal appearing at the depth range of 340–370 km, which is more prominent along 21.5°N, exhibits different depth variation from the D410. For instance, the D410 is uplifted at ~94.5°E–97°E along the south profile while the negative signal above it is generally flat and displays a multi-peak feature east of ~97°E (Figure 4c). Therefore, we consider this signal as a real low-velocity layer atop the D410, rather than a sidelobe artifact that the slowness weighted algorithm fails to eliminate. Despite being less obvious in the north profile, probably due to its spatially variable nature, this negative phase is well separated from the deeper D410 phase in the CCP stacked profiles (Figures 4a and 4b). A low-velocity zone atop the D410 has been reported by several studies and is commonly thought to be induced by partial melting of water- or carbonate-bearing silicates accumulated above the MTZ (e.g., Courtier & Revenaugh, 2007; Song et al., 2004). Another continuous negative signal appears at a depth range of 600–630 km and shows different features from the deeper D660. It is found at a greater depth in the north profile than that in the south. Moreover, this negative phase seems less connected at 94°E–96°E along 23.5°N, whereas the D660 is more continuous and prominent (Figures 4b and 4d). Previous studies interpret the negative phase atop the D660 as a low-velocity layer related to either the accumulation of ancient subducted oceanic material or increased water content at the base of the MTZ (e.g., Y. Shen & Blum, 2003; X. Shen et al., 2014).

Figure 6 shows topographic maps of the D410 and the D660 obtained with the 1-D and 3-D velocity models, where variations in discontinuity depths are clearly visible. One of the most remarkable features is a $2 \times 3^\circ$ area with uplifted D410 in the central part of the study region in both models. The D410 depths obtained with the 1-D model are 15–20 km shallower than standard within 95°E–97°E and 21°N–24°N. To the south and the east of this D410 uplift, the discontinuity depths are locally deeper than normal. In the rest of the study region, the D410 depths are generally close to the global average without significant variations (Figure 6a). The D410 estimated with the 3-D model remains over 15 km uplifted in the central part but the anomaly shifts slightly eastwards in the north (Figure 6b). The D660 topography shows a different pattern than the D410. In the topographic map constructed with the 1-D model, the D660 depths are in the range of 645–660 km west of 97°E, except for a localized anomaly of over 670 km between 20°N and 22°N. No pronounced anomalies are detected in the eastern part (>97°E) (Figure 6c). After taking account of the 3-D velocity heterogeneity, the D660 depression between 93°E and 96°E is enhanced with an average depth of 675 ± 10 km (Figure 6d). Additionally, an uplifted D660 at 96°E–99°E, juxtaposed against the observed D660 depression to the east, is highlighted. We further note that there is a spatial offset between the uplift of D410 and the depression of D660, which will be discussed later.

It is known that, due to lateral heterogeneity in the upper mantle, an inaccurate velocity model could potentially introduce uncertainties into the estimates of absolute depths of MTZ discontinuities. Since the Ps conversions generated at the D410 and the D660 have similar travel paths through the upper mantle, the subtraction of the discontinuity depths, that is, the MTZ thickness, is less dependent on the mantle velocity variations. Figure 6 also shows the MTZ thicknesses beneath Myanmar that were determined with the 1-D and 3-D velocity models. The results with these two models display a similar pattern, which suggests that the MTZ thickness depends less on the velocity model used. The MTZ thickness generally ranges from 230 to 270 km, that is, ± 20 from the standard 250 km. The average MTZ thickness is between ~249 and ~251 km, estimated with the 1-D and 3-D models, respectively. It is comparable to 247 ± 2 km in this area estimated by the global RF study (Lawrence & Shearer, 2006). In the thickness map obtained with the 1-D model, the MTZ is thickened by 15–20 km in the central region from 94°E to 96°E. The MTZ thickness is generally in agreement with the standard value of 250 ± 10 km in the rest of the study region except the two local anomalies at the northwestern end and the southeastern part of the region, where the MTZ thickness is less than 240 km (Figure 6e). The MTZ thickness estimated with the 3-D model (Figure 6f) overall varies to a greater extent than that obtained with the IASP91 model. With nine sparsely distributed IRIS stations, Saikia et al. (2020) also observe a thick MTZ beneath Myanmar.

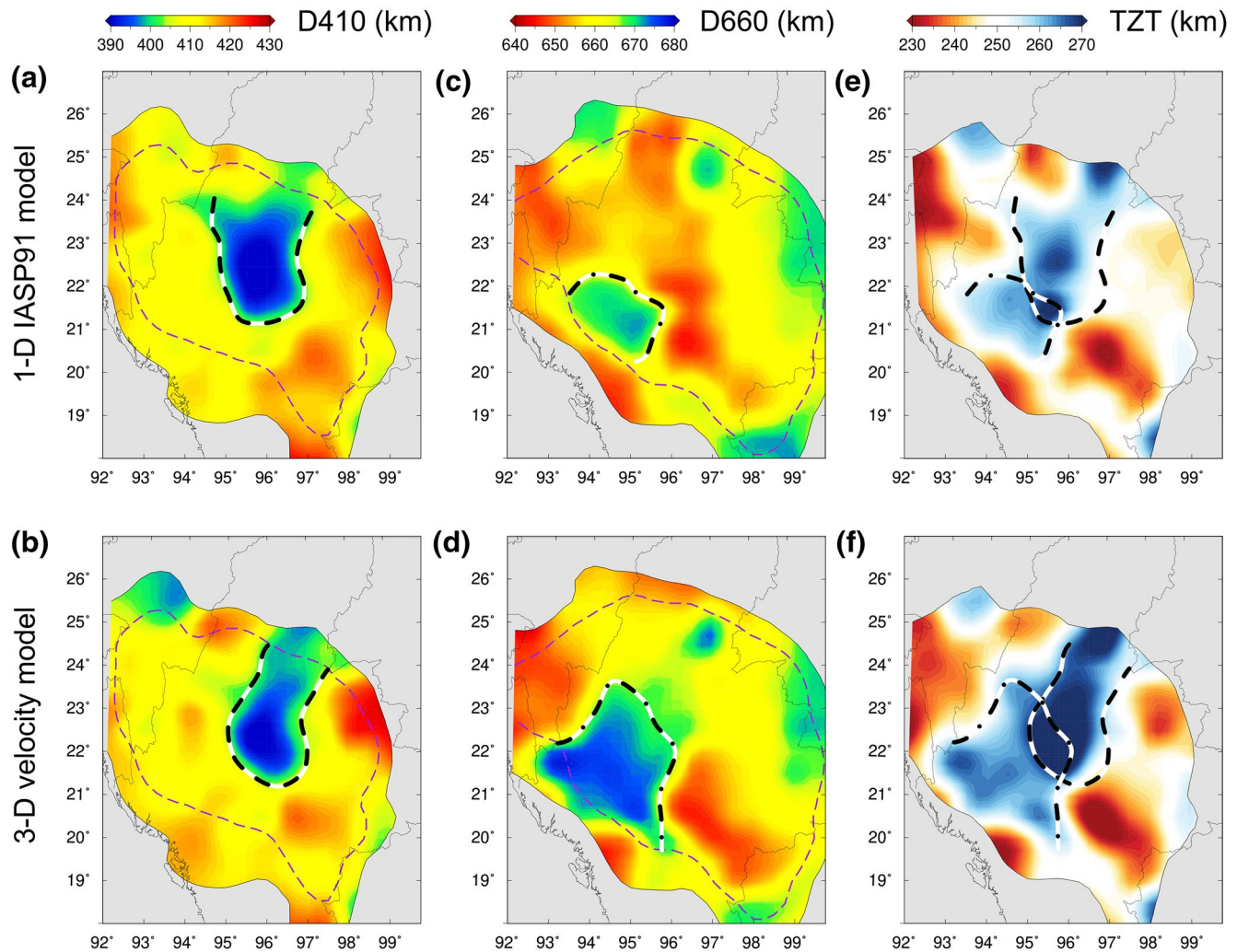


Figure 6. Topographies of the (a, b) D410 and (c, d) D660 determined with the (a, c) 1-D and (b, d) 3-D velocity models. Purple dashed lines outline regions with number of RFs > 100 in each bin at a depth of (a, b) 410 km and >200 at (c, d) 660 km. Corresponding (e, f) thickness maps of the MTZ (TZT) were calculated by subtracting the D410 depth from the D660 depth. Thick dashed and dash-dotted lines outline the regions of the (a, c, e, f) D410 uplift and (c-f) D660 depression, respectively.

4. Discussion

4.1. Robustness of the RF Images

Using the SWCCP stacking approach (Guan & Niu, 2017), we successfully removed most of the multiples that appeared at the MTZ depths in the CCP stacked profiles. The real seismic discontinuities have been thus clearly identified (Figures 4c and 4d). Along the two profiles, we can see waveform variations in width and strength. Apart from processing artifacts, temperature decrease or presence of water could broaden the phase transformation of the D410 and reduce the amplitude (Bina & Helffrich, 1994; Smyth & Frost, 2002). However, in such cases a conversion from the D410 would be less detectable. Alternatively, a broad D410 may be attributed to the lateral smearing of a step-like offset on the mineral phase boundary at the edge of subducted slabs (Schmerr & Garnero, 2007). The nature of waveform changes of the D410 requires further investigation. It is noteworthy that data processing may introduce artifacts. A good epicentral distance distribution is important for effective and unbiased SWCCP stacking. In regions with unsatisfactory data coverage, the Ps conversions in the SWCCP profiles may potentially suffer from energy loss or distortion. For instance, the D660 at both ends of the south profile (21.5°N) displays multiple peaks (Figure 4c). In this study, the SWCCP stacking was applied only to the two west-east oriented profiles, where the RF data are dense.

Since RFs are time series, the time-depth conversion in the CCP stacked profiles depends on the employed velocity model. As a consequence, lateral velocity variations in the crust and upper mantle would cause the depth estimates of the two MTZ discontinuities to shift in the same direction by approximately the same amount (see Figure 5). In topographic maps using a 1-D velocity model, the D660 (Figure 6c) appears to rise simultaneously with the D410 (Figure 6a) within 95°E–97°E and 21°N–24°N but to a much lesser extent. The D660 returns to the global average after the 3-D velocity correction while the D410 remains uplifted (Figures 6b and 6d). To better assess the influence of the 3-D upper mantle structure on the depth estimations of the MTZ discontinuities, we tested two more 3-D models. The first model employs both the 3-D P-wave and S-wave velocity models from Koulakov (2011). The second model adopts the global P-wave velocity model (UU-P07, van der Meer et al., 2018) and a constant perturbation ratio of 1.73 for calculating S-wave velocity. The shallow structure in these two models was replaced by Myanmar Hybrid version 1 (Wang et al., 2019), as applied to the preferred model. The results constructed with both P- and S-velocity models are similar to those obtained with the 1-D velocity model (Figure 6), but the D660 at the longitude range of 93°E–96°E is deepening (Figure S4b). Topographies of the D410 and the D660 constructed with the global UU-P07 model may be overestimated as the D410 and the D660 are simultaneously deeper-than-standard in the southwestern part of the region (Figures S4d and S4e). Nevertheless, the results in all four models (Figures 6 and S4) show first-order consistency of the MTZ discontinuity topographies as well as the MTZ thickness, which verifies the robustness of the major features. Under the assumption that velocity corrections using the 3-D model are accurate enough, it can thus be concluded that our identified features are not artifacts of shallow mantle velocity heterogeneity. Due to the spatial offset between the uplifted D410 and depressed D660, the depth variations of MTZ discontinuities ought to possess more information than the MTZ thickness.

4.2. Eastward Subduction of the Indian Plate

Previous tomographic studies have imaged east-dipping high-velocity anomalies in the mantle and proposed that they represent the eastward subduction of the Indian plate beneath the Burma arc (e.g., Huang & Zhao, 2006; Koulakov, 2011; Lei & Zhao, 2016; Li, van der Hilst, Meltzer, & Engdahl, 2008; Wei et al., 2012). Although detailed images may be inconsistent with each other, the high-velocity Indian slab is clearly visible in all these studies. Some studies suggest that this high-velocity structure continuously extends down to the MTZ (e.g., Wei et al., 2012), whereas others show a gap in the subducted slab between the high-velocity anomaly in the upper mantle and the one in the MTZ (e.g., Bijwaard et al., 1998).

Our D410 topography map reveals an uplift of over 15 km north of ~21°N beneath Myanmar. The spatial distribution of the uplifted D410, constructed with either 1-D or 3-D models (Figures 6a and 6b), has generally a good agreement with the high-velocity anomaly in the tomographic model (Figures 5a and 7a). The simplest explanation for this D410 uplift is the presence of a cold subducted slab inducing a localized low temperature environment. Experimental studies have shown that the Clapeyron slope of the phase transformation across the D410 is positive, with a range from +1.5 to +3.0 MPa/K (Bina & Helffrich, 1994). Assuming a pressure gradient of 35 MPa/km in the upper mantle and a Clapeyron slope of +2.9 MPa/K for the D410 (Bina & Helffrich, 1994), a 15–20 km uplift of the D410 (Figure 6b) corresponds to a 180–240 K negative thermal anomaly. If we further employ a temperature sensitivity of $-0.5\%/100$ K (Cammarano et al., 2003), this thermal anomaly leads to a $\sim 0.9\%$ – 1.2% high-velocity anomaly, which is comparable with the tomographic perturbation (Koulakov, 2011; Figure 7). It can thus be confirmed that the eastward subducted slab beneath Myanmar has penetrated the D410. Recent RF study reports an uplifted 410 below the Andaman Islands (Mishra et al., 2019), suggesting that the Indian slab has also subducted into the MTZ south of our study region.

The D660 topographic map reveals an area of depressed D660 (Figure 6). The depression is enhanced to over 15 km after the 3-D velocity correction (Figure 6d). However, the depressed D660 is offset by ~120 km southwest of the uplifted D410, which makes the MTZ structure under Myanmar different from typical oceanic subduction zones, such as the northwest Pacific subduction zone, where the depressed D660 is immediately below the uplifted D410 or spatially follows the direction of subduction (e.g., Niu et al., 2005). In our study region, the D660 is generally normal below the area where the D410 is uplifted ($>96^\circ\text{E}$). Integrating

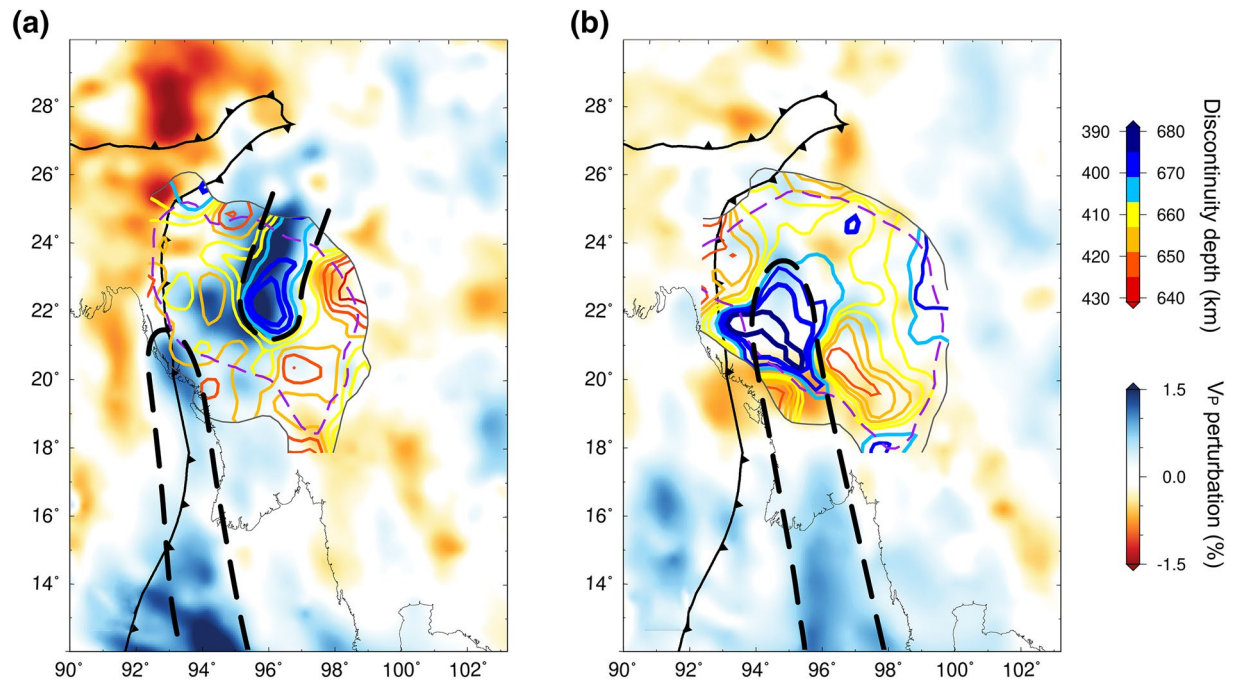


Figure 7. Superposition of P-wave velocity perturbation and topographies of the MTZ discontinuities. Horizontal sections are from the regional P-wave tomographic model (Koulakov, 2011) at (a) 410 km and (b) 650 km depths. Colored contours are topographies of the (a) D410 and (b) D660 determined with the 3-D velocity model. Thick dashed lines outline the two proposed slab segments. See text for more details.

these features, we suggest that after penetrating the D410, the subducted slab was not continuously descending eastwards to the D660. One can speculate that, as the Indian slab kept advancing toward the east, the slab might have coherently buckled backwards after reaching the base of the MTZ and caused the depression of the D660, which we have observed. However, the observed D410 uplift terminates at $\sim 21^\circ\text{N}$ without exceeding farther to the south, which can hardly be explained by continuous slab buckling. In a more feasible scenario, the subducted slab was broken into two parts and a slab window exists between the shallower upper mantle slab and its deeper counterpart. In addition, recent tomographic results show no slab deflection beneath Myanmar (e.g., Koulakov, 2011; Lei & Zhao, 2016; Li, van der Hilst, Meltzer, & Engdahl, 2008; Wei et al., 2012), rather they seem to reveal a slab break-off at the MTZ depths (e.g., Pesicek et al., 2010). Therefore, it is more appropriate to associate the observed offset between the uplifted D410 and depressed D660 anomalies to a slab break-off or tearing process beneath the Burma arc.

4.3. Tearing of the Subducted Slab

Geographically, the Burma arc is located north of the Andaman arc and, therefore, has been commonly considered as an extension of the Andaman oceanic subduction zone. The well-defined Wadati-Benioff zone with intermediate-depth earthquakes down to a depth of ~ 180 km and the associated high-velocity anomalies seen by seismic tomography tend to support that the Burma arc overlies a subducted oceanic slab. In the Central Myanmar Basin late Cenozoic calc-alkaline volcanism has occurred. Lee et al. (2016) identified two distinct eruption stages, implying a change from oceanic to continental subduction. The magmatic stage lasting until the mid-Miocene with typical arc geochemistry is related to the subduction of Indian oceanic lithosphere. After a magmatic gap of >10 million years, the Quaternary stage has more heterogeneous geochemistry by melting in the mantle wedge likely due to slab rollback. The different geometries of the Burma and Andaman arcs imply that they could be separate features. The cloud of intermediate-depth earthquakes terminates to the south at $\sim 20^\circ\text{N}$, clearly separated from the Andaman seismicity (e.g., Pesicek et al., 2010). Seismic tomography, although with limited resolution beneath Myanmar, consistently exhibits a gap between the high-velocity anomalies beneath the Burma arc and those beneath the Andaman arc (e.g., Bijwaard et al., 1998; Koulakov, 2011; Replumaz et al., 2004; van der Meer et al., 2018). At depth of

~220 km beneath the Burma arc, the high-velocity anomalies closely follow the arc-shaped Wadati-Benioff zone (Koulakov, 2011) and separate from the high-velocity anomalies to the south (Bijwaard et al., 1998; Replumaz et al., 2010). Tomographic images from Pesicek et al. (2010) show a transition at ~21°N from a continuous slab throughout the upper mantle and the transition zone beneath the Andaman arc to a slab broken above the MTZ. At MTZ depths, Li, van der Hilst, Engdahl, and Burdick (2008) clearly show a spatial gap between the entire oceanic Sumatra slab and the one beneath the Burma arc. The latter is shifted to the east by ~100 km. These tomographic studies hint at a dramatic change in the subducted slab at 20°N–21°N.

In Figure 7, we superimpose the depth contours of the D410 and the D660 on the tomographic sections at similar depths, respectively. The geometry of the slab-related high-velocity anomaly at the top of the MTZ (Figure 7a) mimics the distribution of Wadati-Benioff zone earthquakes and the volcanic arc (e.g., Bijwaard et al., 1998; Pesicek et al., 2010; Replumaz et al., 2004; van der Meer et al., 2018). North of 21°N, the slab responsible for the D410 uplift (referred to as the Burma slab hereafter) apparently concaves to the east and is disconnected from the slab in the south (referred to as the Andaman slab). Latitude 21°N should mark the southern boundary of both the uplifted D410 and the northern piece of the slab penetrating the D410. Additionally, the upper mantle slab below Myanmar appears to dip less steeply than that in the south, below the Andaman arc (Pesicek et al., 2010). These observations imply that the eastward subducted slab may be torn at 21°N, forming a slab window beneath Myanmar. Even though the slab-shaped high-velocity anomaly can only be seen south of 18°N at the bottom of the MTZ (Figure 7b), possibly due to limited resolution, the observed depression of the D660 by RFs is obvious. Since this depressed D660 is located southwest of the uplifted D410, we suggest that the deeper part of the northernmost Andaman slab shown in Figure 7a probably extends farther north and causes the depression of the D660 in our study region. Such interpretation seems more reasonable than the Burma slab under north central Myanmar deflecting westwards in the MTZ. Instead, the subducted Burma slab north of 21°N may only penetrate the D410 without touching the D660.

Slab tearing has been commonly discussed in the India-Eurasia collision zone, based on sudden change in the velocity anomalies revealed by tomography (Kufner et al., 2016), increased delay time of the shear-wave splitting along certain direction (Chen et al., 2015) and abrupt lateral offset in the LAB evidenced by RFs (Kumar et al., 2016). Slab tearing may trigger thermal upwelling in the mantle. In the MTZ thickness maps constructed with both 1-D and 3-D models, we found a thinner-than-normal MTZ in the southeastern study region juxtaposed against the observed thick MTZ (Figures 6e and 6f). This thin MTZ, corresponding to a depressed D410 and an uplifted D660 immediately below it (Figures 6a–6d), could be the signature of a slab tearing induced mantle upwelling that generates a relatively hot environment. However, more data and further studies, such as upper mantle anisotropy, are required to verify this speculation.

4.4. Subduction Dynamics

Combining the present results with previous observations, we propose a dynamic model under Myanmar. Collision of the Indian plate with Eurasia occurred at ~50 Ma in the western and central Himalayas, while the eastern margin of the convergent system was still dominated by the subduction of the oceanic Neo-Tethys plate at that time (e.g., Hall, 2012; Richards et al., 2007). The subsequent entrance of the buoyant Indian continental lithosphere into the subduction zone along the Burma arc would create an extensional regime in the subducted slab, eventually triggering localization of the deformation, necking, tearing and break-off of the slab (van Hunen & Allen, 2011). The slab break-off probably initiated at a shallow depth in the upper mantle and then developed to the present-day geometry (Figure 8). As India kept moving northwards, the sub-horizontal tear propagated toward the south and a slab window was formed in the upper mantle (Richards et al., 2007; Figure 9a). Subsequently, the deeper part of the Burma slab started to break off, whereas the shallower part of the slab, which was tied to the Indian continent and is more buoyant, became flatter. This would result in upward migration of the tear and thus a more prominent slab window (Figure 9b). As the subduction kept going on, the shallow segment of the Burma slab descended further eastwards to the D410, while the broken-off older oceanic segment sank more sub-vertically down to the D660 (Figures 8 and 9c). This scenario can explain the spatial offset between the depressed D660 and the uplifted D410, as observed by the RFs (Figure 6). Plate reconstruction indicated that during the Late Miocene (12–10 Ma), both the convergent rate and the direction of India toward Eurasia changed rapidly (Molnar & Stock, 2009).

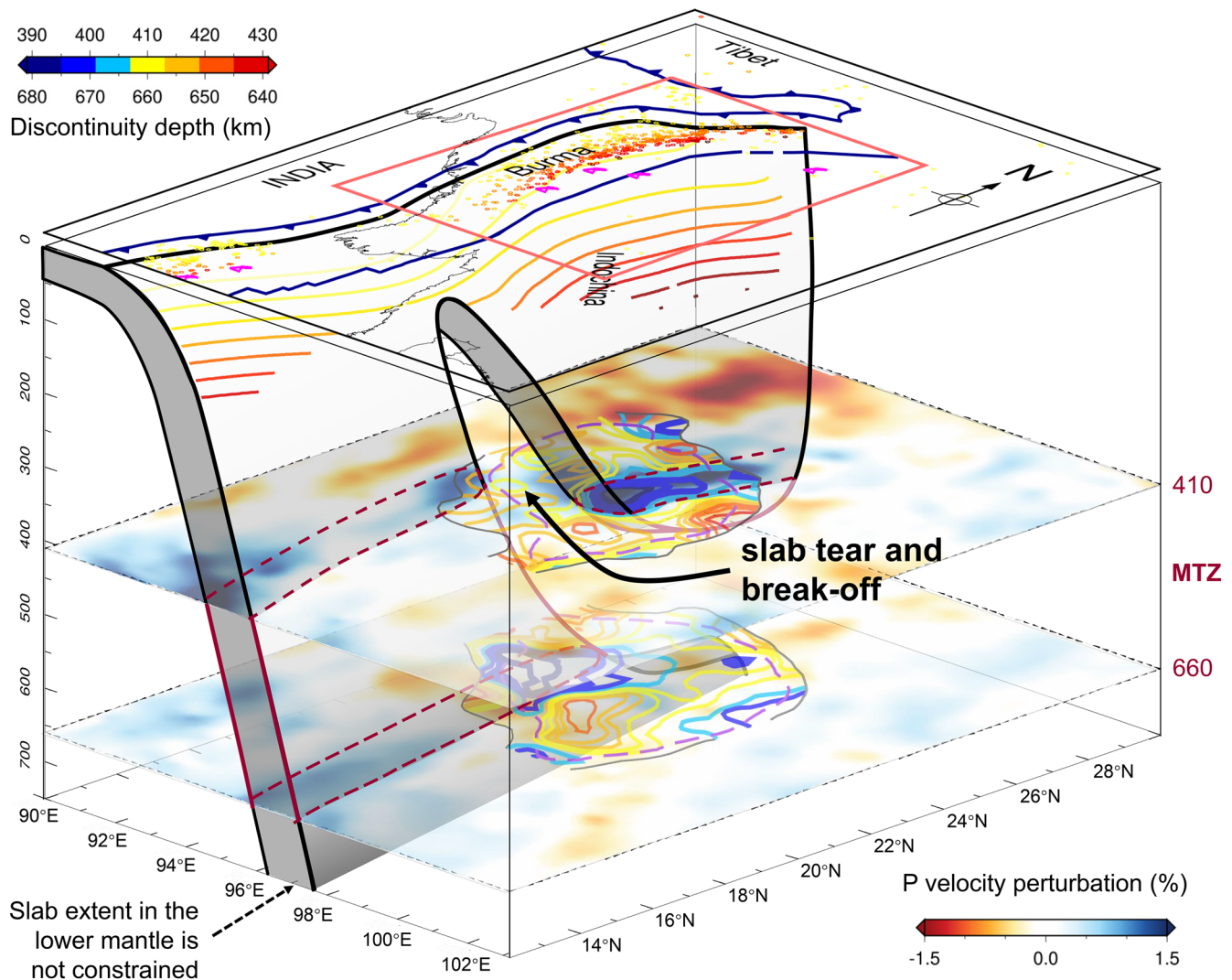


Figure 8. Proposed sketch for the eastward subducted Indian plate. Contours denote topographies of the D410 and the D660 derived from RFs. Underlying horizontal sections are from the regional P-wave tomographic model (Koulakov, 2011) at depths of MTZ boundaries. The southern boundary of the uplifted D410 area suggests a distinct change in slab geometry from north to south. Combining with tomography, we indicate that a slab break-off and tear occurred under Myanmar, forming a slab window. The slab in the north only penetrated the D410 while the slab in the south may have extended to the D660 in our study region. Color maroon highlights the portion of the subducted slab within the MTZ. See Figure 1 and text for more details.

This time period might mark the initiation of the tearing process. After colliding with Eurasia, the convergent rate at the northeast corner of the Indian plate was ~ 4 cm/yr (e.g., Molnar & Stock, 2009; Rangin et al., 2013). However, the subduction along the Burma arc was highly oblique and the Burma plate would probably be mechanically dragged northwards with the Indian plate (Hall, 2012; Maurin & Rangin, 2009). Only part of the convergent rate can thus be attributed to the eastward subduction. Recent GPS study reveals 1.8 cm/yr of west-east convergent rate across the Indo-Burma Ranges (Steckler et al., 2016). Considering an average sinking rate of 2 cm/yr, the slab extending to 600–700 km would correspond to the beginning of plate subduction at around 30–35 Ma, which is roughly consistent with 30–40 Ma estimated by van der Meer et al. (2018).

The nature of subducted slab at the MTZ depths under Myanmar remains unclear. We speculate that the deeper part of the subducted slab hanging in the middle of the MTZ may still preserve its oceanic root, dragging the slab downwards. However, the shallower part, possibly including the depth range of the intermediate-depth earthquakes, may be continental. The slab tear at latitude 21°N might represent a transition from the oceanic Andaman-Sumatra slab in the south to the continental (at least the shallow part) Burma slab in

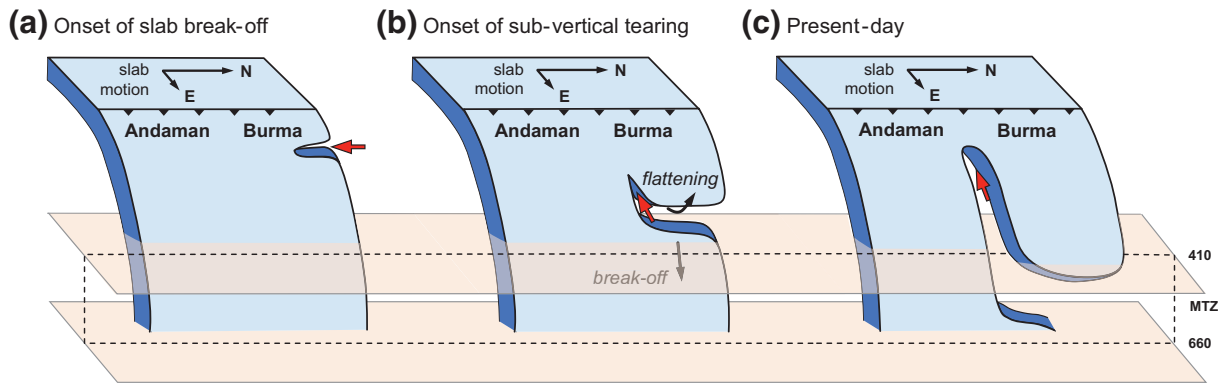


Figure 9. Time evolution of the proposed eastward subducting system beneath Myanmar. (a) Slab break-off nucleated in one point of the slab and then propagated toward the south. (b) Sub-vertical tearing was triggered by break-off of the deeper part of the Burma slab and flattening of its shallower counterpart. (c) Preferred present-day slab geometry that is adopted to interpret the observed disposition of the uplifted D410 and the depressed D660 beneath Myanmar. The red arrow in each schematic indicates the direction of tear migration. Slab extent in the lower mantle is not shown. See text for more details.

the north, which is supported by a recent RF study, suggesting deep subduction of the Indian continental plate north of 21°N (Zheng et al., 2020). Whereas the Andaman slab is subducted into the lower mantle, the Burma slab is broken off, as also seen by seismic tomography (e.g., Pesicek et al., 2010). Most likely, the slab break-off has occurred at a shallower depth and propagated to the D410 depth today during the continuous indentation of the Indian plate. Although slab tearing is most likely to occur at the transitional part of the subducted continent to its leading oceanic slab (van Hunen & Allen, 2011), it seems difficult for the buoyant continental Indian plate alone to subduct deeply into the MTZ and to induce such significant anomaly in the D410 depth, unless the buoyant crust is partly removed from the denser subcontinental lithosphere (Capitanio et al., 2010). Alternatively, a previous study interpreted the high-velocity anomaly appearing beneath Myanmar as an independent micro-plate originally belonging to the northeastern margin of the Greater Indian continent, which was sliding around the eastern Himalayan syntaxis during the Indian plate indentation (Replumaz et al., 2010). In any case, we can confirm that the subducted slab has penetrated the D410 under Myanmar. Our RF observations also indicate a slab gap at ~21°N, where the eastward subducted slab is torn into two parts. The north, shallow-extended slab may be responsible for the uplifted D410 while the depressed D660 is attributed to the broken-off segment connected to the subducted slab below the Andaman arc. However, it is negotiable whether the slab subducted to the D660 in our study region represents the more recent oceanic Indian slab (Replumaz et al., 2004) or a remnant Tethyan slab (Van der Voo et al., 1999).

5. Conclusions

We applied the P-wave RF method to investigate the MTZ discontinuity structure beneath Myanmar. The CCP stacked images, constructed with both 1-D and 3-D velocity models, reveal a 2° × 3° area where the D410 is uplifted by over 15 km in central part of our study region. This feature is in good agreement with the east-dipping high-velocity structure in the tomographic model, suggesting that the subducted slab has penetrated the D410. The southern boundary of the uplifted D410 region at around 21°N indicates a striking change in slab geometry from north to south. Our study also observed a region with depressed D660, which is surprisingly offset to the southwest of the uplifted D410. Combining our findings with results from seismicity and tomography, we propose that the eastward subducted slab may be torn under Myanmar. The slab north of 21°N has penetrated the D410 but may not yet reach the D660, while the broken-off segment in the south may have continuously descended to the bottom of the MTZ.

The present study shows solid evidence for the depth extent of the eastward subducted slab under Myanmar and provides new insights on the geodynamic process of the India-Eurasia collision as well as the tectonic evolution of the eastern Himalayan syntaxis region. However, it is commonly understood that estimating the true depths of the MTZ discontinuities by RFs requires a background velocity model with sufficient spatial resolution covering the entire study region. A well-determined 3-D velocity model with data from

regional networks in Myanmar is not yet available. Therefore, further studies and deployment of dense seismic networks in Myanmar and surrounding regions are urgently needed for better confining the north-south extent of the uplifted D410 and the depressed D660 observed in our study region.

Data Availability Statement

Seismic waveform data were provided by Seismic Array Laboratory at the Institute of Geology and Geophysics, Chinese Academy of Sciences (IGGCAS) (<http://doi.org/10.12129/IGGSL.Data.Observation>), Earth Observatory of Singapore (EOS) (<https://earthobservatory.sg/resources/data/myanmar-velocity-model-v1>), and Incorporated Research Institutions for Seismology (IRIS) (<https://www.iris.edu/hq/>). Receiver function data used in this study can be downloaded via <http://www.dx.doi.org/10.12197/2020GA018>. We used SeismicHandler (Stammler, 1993) for data processing. Most figures in this paper were generated by the Generic Mapping Tools (GMT) (Wessel et al., 2013).

Acknowledgments

We acknowledge all the participants in the CMGSMO project for installing and maintaining the seismic network. We thank Stephan Sobolev and Bernhard Steinberger for constructive comments and Wei Wei for sharing the tomographic model. This study is supported by National Natural Science Foundation of China (41490612), the Strategic Priority Research Program (B) of Chinese Academy of Sciences (XDB18000000) and the International Partnership Program of the Chinese Academy of Sciences (GJHZ1776). Y. Bai is supported by China Scholarship Council (201804910411).

References

- Berkhout, A. J. (1977). Least-squares inverse filtering and wavelet deconvolution. *Geophysics*, 42(7), 1369–1383. <https://doi.org/10.1190/1.1440798>
- Bijwaard, H., Spakman, W., & Engdahl, E. R. (1998). Closing the gap between regional and global travel time tomography. *Journal of Geophysical Research*, 103(B12), 30055–30078. <https://doi.org/10.1029/98JB02467>
- Bina, C. R., & Helffrich, G. (1994). Phase transition Clapeyron slopes and transition zone seismic discontinuity topography. *Journal of Geophysical Research*, 99(B8), 15853–15860. <https://doi.org/10.1029/94JB00462>
- Cammarano, F., Goes, S., Vacher, P., & Giardini, D. (2003). Inferring upper-mantle temperatures from seismic velocities. *Physics of the Earth and Planetary Interiors*, 138(3–4), 197–222. [https://doi.org/10.1016/S0031-9201\(03\)00156-0](https://doi.org/10.1016/S0031-9201(03)00156-0)
- Capitanio, F. A., Morra, G., Goes, S., Weinberg, R. F., & Moresi, L. (2010). India–Asia convergence driven by the subduction of the Greater Indian continent. *Nature Geoscience*, 3(2), 136–139. <https://doi.org/10.1038/ngeo725>
- Chen, Y., Li, W., Yuan, X., Badal, J., & Teng, J. (2015). Tearing of the Indian lithospheric slab beneath southern Tibet revealed by SKS-wave splitting measurements. *Earth and Planetary Science Letters*, 413, 13–24. <https://doi.org/10.1016/j.epsl.2014.12.041>
- Courtier, A. M., & Revenaugh, J. (2007). Deep upper-mantle melting beneath the Tasman and Coral Seas detected with multiple ScS reverberations. *Earth and Planetary Science Letters*, 259(1), 66–76. <https://doi.org/10.1016/j.epsl.2007.04.027>
- Duan, Y., Tian, X., Liang, X., Li, W., Wu, C., Zhou, B., & Iqbal, J. (2017). Subduction of the Indian slab into the mantle transition zone revealed by receiver functions. *Tectonophysics*, 702, 61–69. <https://doi.org/10.1016/j.tecto.2017.02.025>
- Eagar, K. C., Fouch, M. J., & James, D. E. (2010). Receiver function imaging of upper mantle complexity beneath the Pacific Northwest, United States. *Earth and Planetary Science Letters*, 297(1–2), 141–153. <https://doi.org/10.1016/j.epsl.2010.06.015>
- Efron, B., & Tibshirani, R. (1986). Bootstrap methods for standard errors, confidence intervals, and other measures of statistical accuracy. *Statistical Science*, 1(1), 54–75. <https://doi.org/10.1214/ss/1177013815>
- Engdahl, E. R., Di Giacomo, D., Sakarya, B., Gkarklaoui, C. G., Harris, J., & Storchak, D. A. (2020). ISC-EHB 1964–2016, an improved data set for studies of Earth structure and global seismicity. *Earth and Space Science*, 7(1), e2019EA000897. <https://doi.org/10.1029/2019ea000897>
- Gripp, A. E., & Gordon, R. G. (2002). Young tracks of hotspots and current plate velocities. *Geophysical Journal International*, 150(2), 321–361. <https://doi.org/10.1046/j.1365-246X.2002.01627.x>
- Guan, Z., & Niu, F. (2017). An investigation on slowness-weighted CCP stacking and its application to receiver function imaging. *Geophysical Research Letters*, 44(12), 6030–6038. <https://doi.org/10.1002/2017GL073755>
- Hall, R. (2012). Late Jurassic–Cenozoic reconstructions of the Indonesian region and the Indian Ocean. *Tectonophysics*, 570–571(10), 1–41. <https://doi.org/10.1016/j.tecto.2012.04.021>
- Hayes, G. P., Moore, G. L., Portner, D. E., Hearne, M., Flamme, H., Furtney, M., & Smoczyk, G. M. (2018). Slab2, a comprehensive subduction zone geometry model. *Science*, 362(6410), 58–61. <https://doi.org/10.1126/science.aat4723>
- Helffrich, G. (2000). Topography of the transition zone seismic discontinuities. *Reviews of Geophysics*, 38(1), 141–158. <https://doi.org/10.1029/1999RG000060>
- Houser, C., Masters, G., Flanagan, M., & Shearer, P. (2008). Determination and analysis of long-wavelength transition zone structure using SS precursors. *Geophysical Journal International*, 174(1), 178–194. <https://doi.org/10.1111/j.1365-246X.2008.03719.x>
- Huang, J., & Zhao, D. (2006). High-resolution mantle tomography of China and surrounding regions. *Journal of Geophysical Research*, 111, B09305. <https://doi.org/10.1029/2005JB004066>
- Hurukawa, N., Tun, P. P., & Shibazaki, B. (2012). Detailed geometry of the subducting Indian Plate beneath the Burma Plate and crustal seismicity in the Burma Plate derived from joint hypocenter relocation. *Earth, Planets and Space*, 64(4), 333–343. <https://doi.org/10.5047/eps.2011.10.011>
- Kennett, B. L. N., & Engdahl, E. R. (1991). Traveltimes for global earthquake location and phase identification. *Geophysical Journal International*, 105(2), 429–465. <https://doi.org/10.1111/j.1365-246X.1991.tb06724.x>
- Kind, R., Yuan, X., Saul, J., Nelson, D., Sobolev, S. V., Mechie, J., et al. (2002). Seismic images of crust and upper mantle beneath Tibet: Evidence for Eurasian plate subduction. *Science*, 298(5596), 1219–1221. <https://doi.org/10.1126/science.1078115>
- Koulakov, I. (2011). High-frequency P and S velocity anomalies in the upper mantle beneath Asia from inversion of worldwide traveltime data. *Journal of Geophysical Research*, 116, B04301. <https://doi.org/10.1029/2010JB007938>
- Kufner, S.-K., Schurr, B., Sippl, C., Yuan, X., Ratschbacher, L., Arib, A. M. A., et al. (2016). Deep India meets deep Asia: Lithospheric indentation, delamination and break-off under Pamir and Hindu Kush (Central Asia). *Earth and Planetary Science Letters*, 435, 171–184. <https://doi.org/10.1016/j.epsl.2015.11.046>
- Kumar, P., Srijayanthi, G., & Ravi Kumar, M. (2016). Seismic evidence for tearing in the subducting Indian slab beneath the Andaman arc. *Geophysical Research Letters*, 43(10), 4899–4904. <https://doi.org/10.1002/2016gl068590>

- Langston, C. A. (1979). Structure under Mount Rainier, Washington, inferred from teleseismic body waves. *Journal of Geophysical Research*, 84(B9), 4749–4762. <https://doi.org/10.1029/JB084iB09p04749>
- Lawrence, J. F., & Shearer, P. M. (2006). A global study of transition zone thickness using receiver functions. *Journal of Geophysical Research*, 111, B06307. <https://doi.org/10.1029/2005JB003973>
- Lawrence, J. F., & Shearer, P. M. (2008). Imaging mantle transition zone thickness with SdS-SS finite-frequency sensitivity kernels. *Geophysical Journal International*, 174(1), 143–158. <https://doi.org/10.1111/j.1365-246X.2007.03673.x>
- Lee, H.-Y., Chung, S.-L., & Yang, H.-M. (2016). Late Cenozoic volcanism in central Myanmar: Geochemical characteristics and geodynamic significance. *Lithos*, 245, 174–190. <https://doi.org/10.1016/j.lithos.2015.09.018>
- Lei, J., & Zhao, D. (2016). Teleseismic P-wave tomography and mantle dynamics beneath Eastern Tibet. *Geochemistry, Geophysics, Geosystems*, 17(5), 1861–1884. <https://doi.org/10.1002/2016GC006262>
- Li, C., van der Hilst, R. D., Engdahl, E. R., & Burdick, S. (2008). A new global model for P wave speed variations in Earth's mantle. *Geochemistry, Geophysics, Geosystems*, 9, Q05018. <https://doi.org/10.1029/2007GC001806>
- Li, C., van der Hilst, R. D., Meltzer, A. S., & Engdahl, E. R. (2008). Subduction of the Indian lithosphere beneath the Tibetan Plateau and Burma. *Earth and Planetary Science Letters*, 274(1–2), 157–168. <https://doi.org/10.1016/j.epsl.2008.07.016>
- Maurin, T., Masson, F., Rangin, C., Min, U. T., & Collard, P. (2010). First global positioning system results in northern Myanmar: Constant and localized slip rate along the Sagaing fault. *Geology*, 38(7), 591–594. <https://doi.org/10.1130/g30872.1>
- Maurin, T., & Rangin, C. (2009). Structure and kinematics of the Indo-Burmese Wedge: Recent and fast growth of the outer wedge. *Tectonics*, 28, TC2010. <https://doi.org/10.1029/2008TC002276>
- Mishra, S., Prajapati, S., & Teotia, S. S. (2019). Mantle Transition Zones (MTZ) discontinuities beneath the Andaman Subduction Zone. *Journal of Asian Earth Sciences*, 191, 104102. <https://doi.org/10.1016/j.jseas.2019.104102>
- Mitchell, A. H. G. (1993). Cretaceous–Cenozoic tectonic events in the western Myanmar (Burma)–Assam region. *Journal of the Geological Society*, 150(6), 1089–1102. <https://doi.org/10.1144/gsjgs.150.6.1089>
- Mitchell, A., Chung, S.-L., Oo, T., Lin, T.-H., & Hung, C.-H. (2012). Zircon U–Pb ages in Myanmar: Magmatic–metamorphic events and the closure of a neo-Tethys ocean? *Journal of Asian Earth Sciences*, 56, 1–23. <https://doi.org/10.1016/j.jseas.2012.04.019>
- Molnar, P., & Stock, J. M. (2009). Slowing of India's convergence with Eurasia since 20 Ma and its implications for Tibetan mantle dynamics. *Tectonics*, 28, TC3001. <https://doi.org/10.1029/2008TC002271>
- Mon, C. T., Gong, X., Wen, Y., Jiang, M., Chen, Q.-F., Zhang, M., et al. (2020). Insight into major active faults in Central Myanmar and the related geodynamic sources. *Geophysical Research Letters*, 47(8), e2019GL086236. <https://doi.org/10.1029/2019gl086236>
- Nábelek, J., Hetényi, G., Vergne, J., Sapkota, S., Kafle, B., Jiang, M., et al. (2009). Underplating in the Himalaya–Tibet collision zone revealed by the Hi-CLIMB experiment. *Science*, 325(5946), 1371–1374. <https://doi.org/10.1126/science.1167719>
- Ni, J. F., Guzman-Speziale, M., Bevis, M., Holt, W. E., Wallace, T. C., & Seager, W. R. (1989). Accretionary tectonics of Burma and the three-dimensional geometry of the Burma subduction zone. *Geology*, 17(1), 68–71. [https://doi.org/10.1130/0091-7613\(1989\)017<0068:ATOBAT>2.3.CO;2](https://doi.org/10.1130/0091-7613(1989)017<0068:ATOBAT>2.3.CO;2)
- Niu, F., Levander, A., Ham, S., & Obayashi, M. (2005). Mapping the subducting Pacific slab beneath southwest Japan with Hi-net receiver functions. *Earth and Planetary Science Letters*, 239(1–2), 9–17. <https://doi.org/10.1016/j.epsl.2005.08.009>
- Pesicek, J. D., Thurber, C. H., Widiyantoro, S., Zhang, H., DeShon, H. R., & Engdahl, E. R. (2010). Sharpening the tomographic image of the subducting slab below Sumatra, the Andaman Islands and Burma. *Geophysical Journal International*, 182(1), 433–453. <https://doi.org/10.1111/j.1365-246X.2010.04630.x>
- Rangin, C., Maurin, T., & Masson, F. (2013). Combined effects of Eurasia/Sunda oblique convergence and East-Tibetan crustal flow on the active tectonics of Burma. *Journal of Asian Earth Sciences*, 76, 185–194. <https://doi.org/10.1016/j.jseas.2013.05.018>
- Replumaz, A., Káráson, H., van der Hilst, R. D., Besse, J., & Tapponnier, P. (2004). 4-D evolution of SE Asia's mantle from geological reconstructions and seismic tomography. *Earth and Planetary Science Letters*, 221(1–4), 103–115. [https://doi.org/10.1016/S0012-821X\(04\)00070-6](https://doi.org/10.1016/S0012-821X(04)00070-6)
- Replumaz, A., Negro, A. M., Guillot, S., & Villaseñor, A. (2010). Multiple episodes of continental subduction during India/Asia convergence: Insight from seismic tomography and tectonic reconstruction. *Tectonophysics*, 483(1–2), 125–134. <https://doi.org/10.1016/j.tecto.2009.10.007>
- Richards, S., Lister, G., & Kennett, B. (2007). A slab in depth: Three-dimensional geometry and evolution of the Indo-Australian plate. *Geochemistry, Geophysics, Geosystems*, 8, Q12003. <https://doi.org/10.1029/2007GC001657>
- Saikia, D., Kumar, M. R., & Singh, A. (2020). Palaeoslab and plume signatures in the mantle transition zone beneath Eastern Himalaya and adjoining regions. *Geophysical Journal International*, 221(1), 468–477. <https://doi.org/10.1093/gji/ggaa012>
- Schmerr, N., & Garnero, E. J. (2007). Upper mantle discontinuity topography from thermal and chemical heterogeneity. *Science*, 318(5850), 623–626. <https://doi.org/10.1126/science.1145962>
- Shen, Y., & Blum, J. (2003). Seismic evidence for accumulated oceanic crust above the 660-km discontinuity beneath southern Africa. *Geophysical Research Letters*, 30(18), 1925. <https://doi.org/10.1029/2003GL017991>
- Shen, X., Yuan, X., & Li, X. (2014). A ubiquitous low-velocity layer at the base of the mantle transition zone. *Geophysical Research Letters*, 41(3), 836–842. <https://doi.org/10.1002/2013GL058918>
- Smyth, J. R., & Frost, D. J. (2002). The effect of water on the 410-km discontinuity: An experimental study. *Geophysical Research Letters*, 29(10), 123–121–123–124. <https://doi.org/10.1029/2001gl014418>
- Song, T.-R. A., Helmberger, D. V., & Grand, S. P. (2004). Low-velocity zone atop the 410-km seismic discontinuity in the northwestern United States. *Nature*, 427(6974), 530–533. <https://doi.org/10.1038/nature02231>
- Stammler, K. (1993). Seismichandler—Programmable multichannel data handler for interactive and automatic processing of seismological analyses. *Computers & Geosciences*, 19(2), 135–140. [https://doi.org/10.1016/0098-3004\(93\)90110-Q](https://doi.org/10.1016/0098-3004(93)90110-Q)
- Steckler, M. S., Mondal, D. R., Akhter, S. H., Seeber, L., Feng, L., Gale, J., et al. (2016). Locked and loading megathrust linked to active subduction beneath the Indo-Burman Ranges. *Nature Geoscience*, 9(8), 615–618. <https://doi.org/10.1038/ngeo2760>
- Taylor, M., & Yin, A. (2009). Active structures of the Himalayan–Tibetan orogen and their relationships to earthquake distribution, contemporary strain field, and Cenozoic volcanism. *Geosphere*, 5(3), 199–214. <https://doi.org/10.1130/GES00217.1>
- van der Meer, D. G., van Hinsbergen, D. J. J., & Spakman, W. (2018). Atlas of the underworld: Slab remnants in the mantle, their sinking history, and a new outlook on lower mantle viscosity. *Tectonophysics*, 723, 309–448. <https://doi.org/10.1016/j.tecto.2017.10.004>
- Van der Voo, R., Spakman, W., & Bijwaard, H. (1999). Tethyan subducted slabs under India. *Earth and Planetary Science Letters*, 171(1), 7–20. [https://doi.org/10.1016/S0012-821X\(99\)00131-4](https://doi.org/10.1016/S0012-821X(99)00131-4)
- van Hunen, J., & Allen, M. B. (2011). Continental collision and slab break-off: A comparison of 3-D numerical models with observations. *Earth and Planetary Science Letters*, 302(1–2), 27–37. <https://doi.org/10.1016/j.epsl.2010.11.035>

- Vinnik, L. P. (1977). Detection of waves converted from P to SV in the mantle. *Physics of the Earth and Planetary Interiors*, 15(1), 39–45. [https://doi.org/10.1016/0031-9201\(77\)90008-5](https://doi.org/10.1016/0031-9201(77)90008-5)
- Wang, X., Wei, S., Wang, Y., Maung, P., Hubbard, J., Banerjee, P., et al. (2019). A 3-D shear wave velocity model for Myanmar region. *Journal of Geophysical Research: Solid Earth*, 124(1), 504–526. <https://doi.org/10.1029/2018JB016622>
- Wei, W., Xu, J., Zhao, D., & Shi, Y. (2012). East Asia mantle tomography: New insight into plate subduction and intraplate volcanism. *Journal of Asian Earth Sciences*, 60, 88–103. <https://doi.org/10.1016/j.jseas.2012.08.001>
- Wessel, P., Smith, W. H. F., Scharroo, R., Luis, J., & Wobbe, F. (2013). Generic mapping tools: Improved version released. *Eos, Transactions American Geophysical Union*, 94(45), 409–410. <https://doi.org/10.1002/2013eo450001>
- Xu, M., Huang, H., Huang, Z., Wang, P., Wang, L., Xu, M., et al. (2018). Insight into the subducted Indian slab and origin of the Tengchong volcano in SE Tibet from receiver function analysis. *Earth and Planetary Science Letters*, 482, 567–579. <https://doi.org/10.1016/j.epsl.2017.11.048>
- Yu, Y., Gao, S. S., Liu, K. H., Yang, T., Xue, M., & Le, K. P. (2017). Mantle transition zone discontinuities beneath the Indochina Peninsula: Implications for slab subduction and mantle upwelling. *Geophysical Research Letters*, 44(14), 7159–7167. <https://doi.org/10.1002/2017GL073528>
- Yuan, X., Heit, B., Brune, S., Steinberger, B., Geissler, W. H., Jokat, W., & Weber, M. (2017). Seismic structure of the lithosphere beneath NW Namibia: Impact of the Tristan da Cunha mantle plume. *Geochemistry, Geophysics, Geosystems*, 18(1), 125–141. <https://doi.org/10.1002/2016gc006645>
- Zhang, R., Wu, Y., Gao, Z., Fu, Y. V., Sun, L., Wu, Q., & Ding, Z. (2017). Upper mantle discontinuity structure beneath eastern and south-eastern Tibet: New constraints on the Tengchong intraplate volcano and signatures of detached lithosphere under the western Yangtze Craton. *Journal of Geophysical Research: Solid Earth*, 122(2), 1367–1380. <https://doi.org/10.1002/2016JB013551>
- Zheng, T., He, Y., Ding, L., Jiang, M., Ai, Y., Mon, C. T., et al. (2020). Direct structural evidence of Indian continental subduction beneath Myanmar. *Nature Communications*, 11(1), 1944. <https://doi.org/10.1038/s41467-020-15746-3>